Creep condition-oriented design of Molybdenum alloys with La_2O_3 addition assisted by microstructure-based crystal plasticity modeling

Jie Kuang[a], Jinyu Zhang[a], Pengming Cheng[a], Gang Liu[a,*], Jun Sun[a,*], Wei Wen[b,*]

a) State Key Laboratory for Mechanical Behavior of Materials, Xi'an Jiaotong University, Xi'an, 710049, P.R. China

b) School of Engineering, Lancaster University, Lancaster, LA1 4YW, UK

Corresponding author at:

Gang Liu: lgsammer@mail.xjtu.edu.cn; Tel: +86 29-8266-3453

Jun Sun: junsun@xjtu.edu.cn; Tel: +86 29-8266-3453

Wei Wen: w.wen2@lancaster.ac.uk

Abstract： Molybdenum (Mo) alloys are essential for applications requiring outstanding mechanical properties at high temperatures across various industrial sectors. Understanding and predicting the creep properties of Mo alloys is crucial for service safety and the design of new materials. This study introduces a physics-based crystallographic model tailored to the characteristic hierarchical microstructure of Mo-La_2O_3 alloys. By sourcing most parameters from existing literature and calibrating others within recommended ranges, the model effectively predicts creep behavior beyond its initial calibration scope. Through the integration of microstructure descriptors, we systematically explored the impact of different microstructural features on creep behavior and identified underlying mechanisms. This analysis yielded two pivotal concepts: the minimum acceptable grain size and the necessary nanoparticle number density. These metrics, readily obtainable from the model, quantify the requisite grain size and nanoparticle content to achieve the target steady-state creep rates for operational demands, thus providing essential insights for the creep condition-oriented design of Mo-La_2O_3 alloys. The model is also expected to be adaptable for developing other Mo alloys reinforced by second phase particles, aimed at achieving desired creep properties under specified conditions, assuming that relevant parameters are accessible through literature or lower-scale simulations.

Keywords: Molybdenum (Mo) alloys; La_2O_3 particle; Creep property; Crystal plasticity

1 Introduction

Molybdenum (Mo) alloys are critical for applications that demand exceptional mechanical properties at high temperatures [1-3]. Their utilization spans across aerospace for turbine blades and rocket nozzles, nuclear reactors for core components, and electronics for high-temperature filaments and contacts[4]. These sectors benefit from Mo alloys' inherent high-temperature strength and creep resistance, enabling their use in environments where performance and reliability are paramount [5].

Despite their robust performance, the escalating demands of technological applications have necessitated enhancements to traditional Mo alloys, especially in terms of their creep resistance at elevated temperatures [1]. This challenge has sparked interest in doping Mo alloys with oxides such as La_2O_3, Y_2O_3, CeO_2 to boost their performance [6-12]. Among these, lanthanum oxide (La2O3) has been particularly effective, leading to the development of Mo-La_2O_3 alloys with outstanding creep resistance. For example, Mo-La2O3 alloys have demonstrated remarkably low stable creep rates of 3.8×10^{-6} h^{-1} at temperatures as high as 1600 °C when the applied stress was ~34 MPa, outperforming other Mo-oxide alloys [13]. This advancement suggests optimizing the microstructure of Mo-La_2O_3 offers a viable path for Mo alloys to fulfill the rigorous demands of future high-performance applications.

In terms of long-term service, a comprehensive understanding of the creep behavior of Mo-La_2O_3 alloy under operational conditions is indispensable prior to their deployment. Yet, the prolonged nature of creep testing makes such studies significantly less common

than those focusing on quasi-static mechanical properties. For instance, the latest systematic study on the creep behavior of Mo-La_2O_3 alloy was published in 2022 by our group [14], with prior significant studies dating back to the early 2000s [15] and even the late 1990s [13, 16]. This two-decade gap, to some degree, underscores the scarcity of experimental studies on the creep properties of existing Mo-La_2O_3 materials. Moreover, the lengthy duration of creep tests can significantly delay the development cycle of new materials. Not to mention that in many real-world applications, components are subjected to complex stress states that are challenging (sometimes even impossible) to precisely replicate in laboratory settings [17, 18]. Given these challenges in obtaining reliable creep data for reference, the application of highly-efficient computational techniques to predict key creep characteristics, such as minimum creep rate and creep strain, is more than desirable [19]. If established and proven reliable, these techniques could not only facilitate the selection of appropriate materials for specific high-temperature applications but also assist in the development of new alloys designed to withstand rigorous service conditions.

Historically, the creep behavior of materials has been described using empirical or phenomenological models [20, 21]. Although these models can capture the macroscopic responses of many materials, they usually fall short outside their calibration ranges [22-24]. Furthermore, as these models do not include microstructural parameters, materials with exactly the same composition (but different microstructures) could have two sets of totally different empirical parameters. This prevents the model from providing useful insights into the relationship between microstructure and creep responses. Therefore,

while being widely recognized as simple, reliable, and computationally economical, these models have very large limitations when it is employed for both material selection and new material design.

Physics-based models have been considered as the potential way out of the above plight [25]. For one thing, as their name indicates, all the parameters in the models have clear physical meanings. This means that the values of many parameters can be found in the literature, and for the rest that cannot, they are highly likely to be obtained by other modeling methods such as first principle calculations, molecular dynamic simulations [26], dislocation dynamic simulations [27, 28]. Even for the very few (if there exist any) parameters that cannot be determined by the above two methods, from the their physical meanings, we often know their qualitative relationship with the composition and microstructure [29, 30]. Thus, very often (if not always), they can be shared by materials with similar compositions and microstructures. In this regard, physics-based models facilitate not only interpolation within the calibration range, similar to empirical models, but also allow for extrapolation, predicting material behavior under untested conditions beyond the calibration window [22, 23]. Another big advantage of the physics-based model is the explicit incorporation of microstructural parameters into its formulation. This allows an easy establishment of microstructural effects on creep behaviors, which is more than valuable for new materials design. With these two irreplaceable advantages compared to traditional empirical model, the physics-based creep model, though being far less efficient and with more complex formulations, started to attract increasingly more attention recently in the high-temperature materials community, under the background of

the great leap forward of computational capability in the last two decade thanks to the development of computer science.

It should be noted that while ideally speaking, a unified model applicable to all types of materials is always the ultimate pursuit [25]. In practice, however, due to the extreme complexity in material microstructure and the formation of various hierarchical microstructures, as well as the different deformation mechanisms across different types of materials, at present, specific physics-based creep models are usually dedicated to a certain class of material with qualitatively similar compositions and microstructures. For instance, Mukherjee et al. proposed a multiscale model dedicated to the anisotropic creep response of single-crystal Sn-Ag-Cu solder joint composed of Sn dendrite surrounded by eutectic Sn-Ag phase, based on dislocation mechanics [31]. Wu et al. a developed a microstructure-based creep model for additively manufactured Ni-based super alloys characterized by columnar grain structure and specifically considered the correlation between cavity formation kinetics and creep deformation behavior [32]. Wen et al. proposed a crystallographic thermal creep model for Zr alloys that accounts for the hardening contribution of solutes via their time-dependent pinning effect on dislocations [33]. Zhao et al. proposed a dislocation-based model for the long-term creep behaviors of Grade 91 steel with a special tempered martensitic hierarchical microstructure, with particular emphasis on the particle bypass process and the back stress generated by the subrgrain structures.

To date, despite the critical role of Mo alloys in high-temperature applications,

according to our literature survey, there has been a surprising lack of physics-based modeling studies focused on these materials. This gap in research has hindered the accurate prediction of creep properties and slowed the development of new Mo alloys. In order to bridge this gap, starting from our previous experimental research on Mo-La_2O_3 alloys [14], this study aims to 1) develop a novel physics-based crystal plasticity creep model attentive to the hierarchical microstructure of Mo-La_2O_3 alloys; 2) reveal the activity of different creep mechanisms at various creep conditions; 3) identify the key microstructural feature that govern the creep properties of the alloy across a broad range of conditions, and 4) offer guidelines for the creep-condition-orientated microstructure design of Mo-La_2O_3 alloys, in particular regarding the grain size and the nanoparticle number density. This research forms part of a larger initiative to improve the predictability of mechanical properties and expedite the development of new Mo alloys for both ambient [11, 34-40]and high-temperature applications [14, 41].

2 Experimental procedure

Mo-La_2O_3 alloys were fabricated using powder metallurgy techniques. Initially, pure Mo powders were synthesized by reducing Mo-oxide in a hydrogen environment. These powders were then blended with La_2O_3 particles using the Solid-Liquid (S-L) doping method outlined in our earlier work [34, 35, 38]. We prepared three distinct Mo alloys with varying La_2O_3 content, specifically 0.6, 0.9, and 1.5 wt.%. These mixtures underwent pressureless sintering at 1850 °C for 4 h within a hydrogen atmosphere. Post-sintering, the materials were processed through multiple rolling steps to achieve a final

sheet thickness of 4 mm, followed by annealing at 1500 °C for 1 h.

Creep test specimens, each with a cross-section of 6 mm × 4 mm and a gauge length of 30 mm, were cut from the rolled and annealed sheets using an electrical discharge machine (EDM). Creep testing was conducted in a vacuum furnace-equipped tension creep testing machine. Specimen temperatures were monitored using an infrared thermometer, and a high vacuum of 6.67×10^{-3} Pa was maintained by a diffusion pump system. The samples were attached to guidance rods that protruded from the high-temperature chamber and connected to a linear variable differential transformer (LVDT) to record the creep strain. Tests were carried out under constant loads at varying temperatures ranging from 1000 to 1400 °C ((0.4–0.6) T_m), increasing by 100 °C interval. Loads were carefully chosen to achieve steady creep strain rates between 10^{-8} s^{-1} and 10^{-4} s^{-1}. The steady-state creep rates were determined by analyzing the experimental creep strain versus time curve.

3 Modeling framework

3.1 Modeling microstructure

Following the fabrication route as detailed above, the three Mo-La_2O_3 alloys studied in this work have similar hierarchical microstructures. The representative cross-scale characterization results are given in Fig. 1. (Readers are referred to our previous publication [14] for the detailed microstructure characterization of each alloy). The alloys feature a recrystallized microstructure with slightly elongated grains and a typical BCC rolling texture, which aligns with the described fabrication process. The La_2O_3 particles

within these alloys can be categorized, according to size and location, into three types: 1) micron-scale particles predominantly at grain boundaries; 2) submicron-scale particles mainly at subgrain boundaries; and 3) nanoparticles mostly dispersed throughout the subgrain interiors. For a detailed comparison of these microstructural features across alloys with varying La_2O_3 contents, please see Table 1.

3.2 Mechanistic constitutive model

For computational efficiency, the modeling approach of this work is implemented in the mean-field Visco-Plastic Self-Consistent (VPSC) framework [42], despite of its adaptability into full-field method such as finite element modeling. The deformation of each grain is determined based on crystal plasticity theory and addresses the stress-strain response on each slip/climb system. Considering the coarse grain size, the existence of large numbers of intergranular La_2O_3 particles and the medium creep temperature, grain boundary sliding is not considered in the present model. Hence, the plastic strain rate tensor of each grain ($\dot{\varepsilon}^p$) contains the contributions of dislocation glide ($\dot{\varepsilon}^d$), dislocation climb ($\dot{\varepsilon}^c$) and diffusional creeps including Coble creep ($\dot{\varepsilon}^{coble}$) and Nabarro-Herring (NH) creep ($\dot{\varepsilon}^{N-H}$):

$$\dot{\boldsymbol{\varepsilon}}^p = \dot{\boldsymbol{\varepsilon}}^d + \dot{\boldsymbol{\varepsilon}}^c + \dot{\boldsymbol{\varepsilon}}^{coble} + \dot{\boldsymbol{\varepsilon}}^{N-H} \quad (1)$$

3.2.1 Dislocation glide

The contribution of dislocation glide can be determined using classic crystal plasticity theory as follows:

$$\dot{\varepsilon}_{ij}^d = \sum_s m_{ij}^s \bar{\dot{\gamma}}^s \quad (2)$$

where $m_{ij}^s = \frac{1}{2}\left(n_i^s b_j^s + n_j^s b_i^s\right)$ is the symmetric part of the Schmid tensor, with $\boldsymbol{b}^s$ and $\boldsymbol{n}^s$ representing Burgers vector and the normal direction of the slip plane, respectively. $\bar{\dot{\gamma}}^s$ denotes the mean shear rate of slip system *s* in a grain.

To account for the intragranular stress fluctuation caused by the hierarchical microstructural features such as La_2O_3 nanoparticles and subgrain boundaries, Following the theory originally proposed by Wang et al. [43, 44], we divided each grain into an infinite number of sub-material points, each with its own local stress and the corresponding strain rate. The intragranular stress fluctuation is expressed as the superposition of the elastic stress fields around all the dislocations. Accordingly, the average shear rate of the slip system s in the grain domain ($\bar{\dot{\gamma}}^s$) can be expressed as:

$$\bar{\dot{\gamma}}^s = \int_{-\infty}^{\infty} \dot{\gamma}^s(\tau^s) P(\tau^s - \bar{\tau}^s) d\tau^s \tag{3}$$

where $\dot{\gamma}^s$ is the local shear rate of slip system s, calculated as a function of local resolved shear stress τ^s. The probability distribution function $P(\tau^s - \bar{\tau}^s)$, denoting the volume fraction of the sub-material points with specific local stress τ^s, is represented by the Gaussian distribution as:

$$P(\tau^s - \bar{\tau}^s) = \frac{1}{\sqrt{2\pi V}} \exp\left(-\frac{(\tau^s - \bar{\tau}^s)^2}{2V^2}\right) \tag{4}$$

V is the distribution variance. $\bar{\tau}^s = \boldsymbol{\sigma}:\boldsymbol{m}$ refers to the mean resolved shear stress of slip system *s* in a grain, where $\boldsymbol{\sigma}$ is the deviatoric Cauchy stress tensor. The local shear rate due to the dislocation slip of slip system *s* ($\dot{\gamma}^s$), can be expressed via Orowan's equation:

$$\dot{\gamma}^s = \rho_{cell}^s b v^s sign(\tau^s) \tag{5}$$

where ρ_{cell}^s is the density of mobile dislocation of system *s* in the interior of the subgrain

(cell). b is the magnitude of Burger's vector. $v^s = \lambda^s / t_w^s$ denotes the mean dislocation velocity, which is determined by the dislocation mean free path (λ^s), and the average time the mobile dislocation spent at obstacles before bypassing (t_w^s) takes place. Note that theoretically, the dislocation mean velocity should be determined by the sum of the dislocation travel time between obstacles and the waiting time before it bypass an obstacle. However, for the low strain rate deformation in this work, the former is negligible in comparison to the latter. Therefore, it is not taken into consideration.

The dislocation mean free path λ^s represents the mean distance between obstacles. In the present work, two types of obstacles are accounted for, namely La_2O_3 particles and other dislocations within the grain. Therefore, λ^s can be expressed as the harmonic mean of the mean spacing for each type of obstacle:

$$\lambda^s = \left(\frac{1}{\lambda_{p,cell}^s} + \frac{1}{\lambda_{\rho,cell}^s} \right)^{-1} \text{ with } \lambda_{\rho,cell}^s = \frac{1}{\sqrt{\sum_s \alpha^{ss'} \rho_{cell}^s}} \text{ and } \lambda_p^s = \frac{1}{h_p \sqrt{N_{p,cell} D_{p,cell}}} \tag{6}$$

where $\lambda_{p,cell}^s$ and $\lambda_{\rho,cell}^s$ refer to the mean spacing for La_2O_3 particles and dislocations within the subgrain, respectively. $\alpha^{ss'}$ is the latent hardening matrix describing the interaction between dislocations from slip systems s and s'. $N_{p,cell}$ and $D_{p,cell}$ are the the number density and mean size of the La_2O_3 particles in the subgrain, which can be obtained from Table 1.

The dislocation glide is essentially a series of thermally activated obstacle-bypass processes. The waiting time a mobile dislocation spent at the obstacles before bypassing can be expressed using the Arrhenius equation [30]:

$$t_{w,i}^{s} = \frac{1}{\upsilon_i}\exp(\frac{\Delta G_i^s}{kT}) \tag{7}$$

where υ_i and ΔG_i^s are, respectively, the attempt frequency and the stress-dependent activation energy to bypass La_2O_3 particles ($i = P$) or other dislocations ($i = \rho$). k and T are the Boltzmann constant and temperature, respectively. The attempt frequency for particle obstacles υ_p is regarded as a constant, whereas the attempt frequency for dislocation obstacles υ_ρ is suggested to be dependent on the dislocation traveling velocity (approximated by the shear wave velocity C_s), an entropy factor χ_e (of the order of unity) and the average length of the vibrating dislocation segments (represented by dislocation mean free path λ_s) [45]. It can be determined as:

$$\upsilon_\rho = \chi_e C_s/\lambda^s \tag{8}$$

The average waiting time considering both obstacles can be obtained as:

$$t_w^s = P_\rho t_{w,\rho}^s + (1 - P_\rho)t_{w,P}^s \tag{9}$$

with P_ρ denoting the probability of encountering a dislocation obstacle, given as:

$$P_\rho = \frac{1}{\lambda_{\rho,cell}^s}/\frac{1}{\lambda^s} \tag{10}$$

The activation energy in Eq. (7) can be expressed as:

$$\Delta G_i^s = \begin{cases} \Delta G_{0,i}\left(1 - \left(\frac{\tau^s}{\tau_{CRSS}^s}\right)^p\right)^q, if \ \ \tau^s < \tau_{CRSS}^s \\ 0 \qquad\qquad\quad , if \ \ \tau^s \geq \tau_{CRSS}^s \end{cases} \tag{11}$$

$\Delta G_{0,i}$ refers to the activation energy without externally applied stress. p and q are exponent parameters describing the obstacle resistance profile. τ_{CRSS}^s denotes the critical resolved shear stress (CRSS). It captures the slip resistance on system s due to both short-range and long-range effects. Therefore, the contribution of all dislocations and La_2O_3 particles in the material (both in the subgrain and on the boundaries) are considered

in τ_{CRSS}^{s} through the superposition [46, 47]:

$$\tau_{CRSS}^{s} = \tau_0 + \left(\left(\tau_{\rho}^{s}\right)^{m} + \left(\tau_{P}^{s}\right)^{m}\right)^{1/m} \tag{12}$$

τ_{P}^{s} is the precipitation hardening term, computed using the dispersed barrier hardening (DBH) model as $\tau_{P}^{s} = h_p \mu b \sqrt{N_p^{cell} D_p^{cell} + N_p^{cw} D_p^{cw} + N_p^{gb} D_p^{gb}}$. N_p^{cw} and D_p^{cw} are the number density and diameter of the La_2O_3 particles decorated on the subgrain boundaries, respectively. N_p^{gb} and D_p^{gb} are the number density and diameter of the La_2O_3 particles reside on the grain boundaries, respectively. The dislocation hardening term τ_{ρ}^{s} is given by the classic Taylor law: $\tau_{\rho} = \mu b \sqrt{\sum_s \alpha^{ss'} (\rho_{cell}^{s'} + \rho_{cw}^{s'})}$. Here ρ_{cw}^{s} refers to the density of dislocations in the subgrain boundary, representing the contribution of subgrain boundaries to the CRSS. Notice that this expression is equivalent to the classic Hall-Petch approach as the subgrain size is proportional to $1/\sqrt{\sum_s \rho_{cw}^{s}}$. According to our previous work [14, 36, 38] and results from other groups [48], The presence of La_2O_3 particles in Mo alloys leads to a strong pinning effect, preventing the annihilation of subgrain structures under the temperatures in the present study. As such, ρ_{cw} is roughly considered as a constant for Mo-La_2O_3 alloy throughout the creep process. Meanwhile, the mobile dislocation density varies according to the Kocks-Mecking law [49]:

$$\dot{\rho}_{cell}^{s} = \frac{k_1}{b\lambda^{s}} |\dot{\bar{\gamma}}^{s}| - f \rho_{cell}^{s} |\dot{\bar{\gamma}}^{s}| \tag{13}$$

where f is the dynamic recovery parameter. Estrin [50] suggested that f is associated with the activities of the dislocation annihilation mechanisms (climb or cross-slip) and can be expressed as:

$$f = k_2 \left(\frac{\dot{\varepsilon}^{0}}{\dot{\varepsilon}}\right)^{1/n_0} \tag{14}$$

where k_1 and k_2 are material constants. $\dot{\varepsilon}^0$ is a reference strain rate, n_0 is the strain rate sensitivity parameter with a value around 3-5 for the high-temperature regime where the dynamic recovery process is mainly controlled by climb [50].

3.2.2 Dislocation climb

Dislocation climb is known as the non-conservative movement of edge dislocations perpendicular to their slip plane through the absorption or emission of point defects. It usually plays a more significant role at high temperatures, attributed to the increased density and diffusivity of vacancies. In this study, a crystal plasticity climb model is employed to quantify the contribution of climb to the creep rate. Similar to dislocation glide, the climb rate can be expressed in the crystal plasticity framework as:

$$\dot{\varepsilon}_{ij}^{c} = \sum_s c_{ij}^s \bar{\dot{\beta}}^s \tag{15}$$

with $c_{ij}^s = b_i^s b_j^s$ being the climb tensor [51]. $\bar{\dot{\beta}}^s$ is the mean climb velocity of edge dislocation within a grain. Similar to Eqs. (3) and (4), it can be determined as the average of local climb rate $\dot{\beta}^s$ over all sub-materials points:

$$\bar{\dot{\beta}}^s = \int_{-\infty}^{\infty} \dot{\beta}^s(\tau_{climb}^s) \frac{1}{\sqrt{2\pi V}} \exp\left(-\frac{(\tau_{climb}^s - \bar{\tau}_{climb}^s)^2}{2V^2}\right) d\,\tau_{climb}^s \tag{16}$$

where τ_{climb}^s denotes the local resolved climb stress in the sub-material points, whereas $\bar{\tau}_{climb}^s = \boldsymbol{\sigma}:\boldsymbol{c}$ is the mean climb stress of a grain. The local climb rate $\dot{\beta}^s$ can also be described using an Orowan-type equation as glide as:

$$\dot{\beta}^s = \rho_{cell,edge}^s b v_c^s sign(\tau_{climb}^s) \tag{17}$$

where $\rho_{cell,edge}^s$ represents the edge mobile dislocation density. In BCC materials, the density of edge dislocation is usually low compared to that of screw dislocations. 10% of mobile dislocations are assumed to be edge ($\rho_{cell,edge}^s = 0.1 \times \rho_{cell}^s$) in this work. The

climb velocity v_c^s is proportional to the net flux of vancacies absorbed or emitted by an edge dislocation segment, which can be determined by analyzing the diffusion process in a cylindrical control volume around a dislocation segment [27-29, 52, 53]. Thus v_c^s can be given as:

$$v_c^s = \frac{2\pi D_V (C_V^\infty - C_V^r)}{b \cdot ln\left(\frac{r^\infty}{r^i}\right)} \tag{18}$$

with r^i and r^∞ being the radius of the inner and outer surfaces of the control volume. C_V^∞ represents the vacancy concentration at the outer surface, which is assumed to be equal to the equilibrium vacancy concentration of the matrix as $C_V^\infty = exp\left(-E_V^f/kT\right)$ with E_V^f the vacancy formation energy. C_V^r is vacancy concentration at the inner surface of the control volume. It can be expressed as follows assuming the equilibrium between the chemical force and the applied climb force is achieved

$$C_V^r = C_V^\infty exp\left(\frac{-\tau_{climb}^s \Omega}{kT}\right) \tag{19}$$

where $\Omega = b^3$ is the atomic volume, $D_V = D_0 exp(-E_V^m/kT)$ in Eq. (18) denotes the vacancy diffusivity at a given temperature. D_0 and E_V^m are the diffusion constant and vacancy migration energy, respectively. Therefore, the expression for climb velocity can be written as:

$$v_c^s = \frac{2\pi D_0 exp\left(\frac{-Q_l}{kT}\right)\left(1 - exp\left(\frac{-\tau_{climb}^s \Omega}{kT}\right)\right)}{b \cdot ln\left(\frac{r^\infty}{r^i}\right)} \tag{20}$$

with $Q_l = E_V^m + E_V^f$ being the diffusion activation energy in the lattice.

3.2.3 Diffusional creep

The diffusional creep mechanisms considered in the present study include Coble and Nabarro-Herring creep. The former describes the creep deformation caused by diffusion

of vacancies along the grain boundaries, while the latter refers to that caused by the diffusion of vacancies through the grain interior. Their relative activities and contributions to the creep rate are dependent on the applied stress, temperature and vacancy diffusivity. Both Coble creep rate $\dot{\varepsilon}_{ij}^{coble}$ [54] and Nabarro-Herring creep rate $\dot{\varepsilon}_{ij}^{NH}$ [55, 56] can be expressed using Arrhenius expressions as follows:

$$\dot{\varepsilon}_{ij}^{coble} = \frac{\alpha_{coble}\sigma_{ij}D_0\delta_{gb}\Omega}{\pi D^3 kT} exp\left(\frac{-Q_{gb}}{kT}\right) \quad (21)$$

$$\dot{\varepsilon}_{ij}^{NH} = \frac{\alpha_{NH}\sigma_{ij}D_0\Omega}{D^2 kT} exp\left(\frac{-Q_l}{kT}\right) \quad (22)$$

where α_{coble} and α_{NH} are constants. δ_{gb} denotes the thickness of grain boundaries, D denotes the mean grain size. Q_{gb} is the vacancy activation energy on the grain boundary, which differs from the activation energy in the lattice (Q_l).

4 Simulation and resultsParameter calibration

Three types of parameters are involved in the present model, namely:

1) Intrinsic material properties: Burgers vector (b), mass density (ρ_{mass}), shear modulus (μ), shear wave velocity (C_s), grain boundary thickness (δ_{gb}), diffusion constant (D_0), lattice diffusion activation energy (Q_l), and grain boundary diffusion activation energy (Q_{gb}).

2) Initial microstructure descriptors: grain size (D); diameter of particles in the interior the subgrain , on the subgrain boundaries, and on the grain boundaries (D_p^{cell}, D_p^{cw}, and D_p^{gb}); the number density of the particles within subgrains, on the subgrain boundaries, and on the grain boundaries (N_p^{cell}, N_p^{cw}, and N_p^{gb}); the dislocation density within subgrains and within subgrain boundaries (ρ_{cell}^s and ρ_{cw}^s); the

crystallographic texture of the material.

3) Model specific parameters: lattice friction (τ_0), hardening superposition exponent (m), the inner and outer radius of dislocation control volume (r_d and r_∞), the attempt frequency of dislocations to bypass particle obstacles (ν_p), entropy factor (χ_e), Gaussian distribution variance (V), annihilation strain rate sensitivity (n_0), the exponent determines the shape of the obstacle resistance profile (p and q), the materials constant that governs the dislocation annihilation (k_1 and k_2), the Coble creep constant (α_{Coble}) and N-H creep constant (α_{NH}), the Zero-stress activation energy for bypassing dislocation obstacles ($\Delta G_{0,\rho}$) and particle obstacles ($\Delta G_{0,p}$).

For intrinsic material properties, most values, except for the grain boundary diffusion activation energy (Q_{gb}) for Mo, can be sourced from the literature. Since precise values for Q_{gb} has not been reported, it is treated as a fitting parameter, determined based on the transition temperature between Coble creep and N-H creep as reported in the creep (dominant) deformation mechanisms maps [57]. Regarding microstructure descriptors, most parameters are adopted directly from the experiments, with the exception of dislocation density, for which reliable synchrotron X-ray diffraction data are currently unavailable. Hence, dislocation densities are treated as fitting parameters and assumed identical across all three materials studied. For simplification, the initial mobile dislocation density on each slip system is fitted within the range of $1 \times 10^{11}\ m^{-2}$ to $1 \times 10^{12}\ m^{-2}$, resulting in a total dislocation density between $2.4\times 10^{12}\ m^{-2}$ and $2.4\times 10^{13}\ m^{-2}$, which is consistent with the recrystallized microstructure depicted in Fig. 1.

Dislocation density in subgrain boundaries is assumed to be 3 to 20 times as that of the mobile dislocation density. For model-specific parameters, thanks to their physics-based nature, many can be either directly adopted from literature or calculated based on intrinsic material properties. Remaining parameters that cannot be determined through these methods are left as fitting parameters but are kept within a reasonable range as recommended by literature.

Parameter calibration for this study utilized creep rate curves of Mo-0.6wt% La_2O_3 alloys at various stress levels at 1200 °C. Given the optimization process's propensity for yielding multiple viable solutions, several parameter sets acceptably matching the experimental creep curves were initially chosen. These sets were then validated using the initial creep rate of pure Mo, recognizing that our model does not include recrystallization and grain growth, hence it cannot fully replicate the entire creep curve of pure Mo. The parameter set that best matched the experimental data for both the alloy and pure Mo was ultimately adopted. The optimized simulation results, displayed in Fig. 2, closely align with the experimental data up to the onset of tertiary creep. Both the initial and steady-state creep rates, as illustrated in Fig. 2(b), correlate well with the experimental measurements. The deviation from the experimental data during the tertiary creep phase is anticipated since the model does not account for damage nucleation and growth. It's noteworthy that the calibration was limited to Mo-0.6wt% La_2O_3 alloys at 1200 °C and stress levels from 60 to 90 MPa. The black scatter points for pure Mo in Fig. 2(b) were used exclusively for validation. The consistency between the simulation and experiments underscores the reliability of the calibrated parameters. All the parameters (except for the

microstructure descriptors listed in Table 1), are given in Table 2 along with appropriate references, stating explicitly whether the values are adopted from the literature or obtained through calibration. For those parameters that have a reasonable range to be calibrated within, the range is also given for reader's reference.

4.2 Creep response prediction

Utilizing the parameters outlined in Table 2, we simulated the creep response of Mo alloys with varying La_2O_3 additions under different stress levels and temperatures, comparing these simulations against available experimental data. The comparisons are displayed in Fig. 3, which shows that, generally, the simulation predictions align well with experimental outcomes, particularly regarding the steady-state creep rate. Given that the parameter calibration was based solely on creep data from Mo-0.6wt% La_2O_3 at 1200 ℃ and stress levels of 60~90 MPa, the model's ability to accurately predict the behavior of the same material at higher temperatures of 1300~1400 ℃ and stress ranges from 40~80 MPa underscores its effectiveness in capturing the influences of temperature and stress on creep behavior. Additionally, the strong agreement between the simulations and experimental data for Mo-0.9wt% La_2O_3 and Mo-1.5wt% La_2O_3 shows the model's capability to account for microstructural effects on creep behavior. These outcomes demonstrate the model's robustness in describing the impacts of temperature, stress, and microstructure on the creep behaviors of Mo- La_2O_3 alloys, even when operating outside the original calibration window. This ability to extrapolate and accurately capture microstructural effects without adjusting the calibrated parameters is crucial for scenarios

where the model is used to support the microstructure design of new materials.

4.3 Creep stress exponent and apparent activation energy

As illustrated in Fig. 4, by plotting the steady-state creep rate against stress on a double logarithmic scale, we obtain the apparent stress exponent n_{app} based on the curve's slope at different stress levels. For both Mo-0.6wt%La_2O_3 (Table 3) and Mo-1.5wt%La_2O_3 (Table 4), n_{app} generally increases with stress. For example, at 1000 °C, n_{app} gradually rises from approximately 1.4 to 17 as stress increases from 5 MPa to 120 MPa. The relationship between n_{app} and temperature is more complex; below 20 MPa, n_{app} initially increases with temperature, then decreases, with the turning point shifting to lower temperatures as stress increases. Above 60 MPa, n_{app} consistently decreases with temperature across the explored range.

By analyzing the steady-state creep rate versus reciprocal temperature ($1/T$), we determine the apparent activation energy Q_{app} for the creep process at various stress levels. The linear relationship depicted in Fig. 4(c) suggests that the apparent activation energy for the Mo-0.6wt%La_2O_3 alloy is almost consistent across the temperature range of 1000 °C to 1500 °C. This linearity persists for the Mo-1.5wt%La_2O_3 alloy at stress levels above 20 MPa. However, at lower stresses, the plots in Fig. 4(d) show a noticeable deflection at around 1100 °C ($1/T$ ~ 7.28×10^{-4} K^{-1}), signifying a reduction in Q_{app} below this temperature. Additionally, both materials generally exhibit a decreasing trend in Q_{app} with increasing stress levels, though Mo-1.5wt%La_2O_3 shows a slight initial increase from 5 MPa to 10 MPa. Specifically, in the Mo-0.6wt%La_2O_3 alloy, Q_{app}

decreases from 507 kJ/mol at 5 MPa to 350 kJ/mol at 120 MPa. In contrast, the Mo-1.5wt%La2O3 alloy initially increases slightly from 522 kJ/mol at 5 MPa to 525 kJ/mol at 10 MPa, then exhibits a steady decrease to 363 kJ/mol at 120 MPa.

4.4 Relative activities of creep mechanisms

Displayed in Fig. 5 are the simulated relative activities of each creep mechanism for Mo-0.6wt%La_2O_3 and Mo-1.5wt%La_2O_3 across various representative creep conditions. Notably, Coble creep is the predominant mechanism at low temperatures and stresses, such as at 1000 °C and 5 MPa. However, at elevated stresses ranging from 60 to 120 MPa, dislocation slip emerges as the dominant mechanism, regardless of temperature.

Under more typical creep conditions, the deformation process involves the activation of multiple mechanisms. An increase in stress typically shifts the balance towards greater dislocation slip activity, simultaneously diminishing the roles of diffusional mechanisms such as Coble and N-H creep. Dislocation climb, another dislocation-related mechanism, displays complex behavior depending on specific creep conditions. For instance, at 1000 °C, the activity of climb in both Mo-0.6wt%La_2O_3 and Mo-1.5wt%La_2O_3 initially increases from 5 MPa, peaks at 20 MPa, and then decreases at higher stresses, essentially vanishing at 120 MPa. As the temperature is increased to 1200 °C, the non-monotonic trend persists, but the peak shifts to 10 MPa. Elevating the temperature further to 1300 °C and beyond transforms this behavior into a continuous decreasing trend, with relative activities progressively declining as stress increases.

Across all investigated stress levels, the relative activity of Coble creep decreases

with rising temperature. In contrast, the activities related to dislocations, both slip and climb, increase with temperature when the stress is below 20 MPa, yet they become insensitive to further temperature increases at stresses above 60 MPa. This pattern highlights the intricate coupling effect of stress and temperature on the creep mechanisms in Mo-La_2O_3 alloys.

5 Discussion**Creep mechanisms: decrypting the apparent creep activation energy and stress exponent**

The ultimate goal of any creep study is to enhance the material's creep properties, specifically to reduce the creep strain rate under defined service conditions. To accomplish this, it's essential to first understand the causes of creep strain, that is, to identify the creep mechanisms active under particular conditions of interest. This is conventionally achieved by analyzing the apparent stress exponent n_{app} and apparent creep activation energy Q_{app}.

Q_{app} serves as a crucial indicator of the type of creep mechanism at play. For processes dominated by Coble creep, Q_{app} should align with that of grain boundary diffusion Q_{gb}. In cases where N-H creep or dislocation climb prevails, Q_{app} matches that of bulk diffusion Q_l, which is higher than Q_{app}. When dislocation slip is the primary mechanism, the activation energy reflects the energy barriers that dislocations must overcome, such as other dislocations or second-phase particles. The apparent stress exponent n_{app} is another indicator of creep mechanisms. When the creep is dominated by diffusional creep such as Coble creep or N-H creep, n_{app} equals 1. If, on the other

hand, the creep process is dominated by dislocation activities including slip and climb, n_{app} is reported to be 3 and 5~7, respectively. For pure metals and single-phase alloys, n_{app} above 7 typically indicate a power law breakdown. In materials reinforced with second-phase particles, like the present Mo-La_2O_3 alloy, n_{app} greater than 7 is often indicative of strong dislocation-particle interactions, which gives rise to an apparent threshold stress, resulting in a steeper creep rate versus stress response.

The activation energy for lattice diffusion in Mo is reported as ~461 kJ/mol [63]. Hence, the low apparent activation energy observed in Mo-La_2O_3 at stresses below 10 MPa (200–250 kJ/mol) likely stems from grain boundary diffusion involvement. At 1000 °C, together with the near-unity stress exponent (~1.5), this suggests Coble creep being an important contributor to the creep strain. For the creep at stress above 60 MPa, by contrast, the "abnormally" high values of apparent stress exponent and the apparent creep activation energy exceeding that of lattice diffusion, underscores the important role played by dislocation overcoming obstacles during slip.

While the information derived from these analyses is valuable, the fundamental assumption that creep occurs through a dominant mechanism largely limits the method's ability to provide deeper insights, particularly in situations where several creep mechanisms are comparably active. To make our point clear, we consider the same example mentioned above, i.e. 1000 °C and 5 MPa, for which n_{app} is measured to be ~1.5. From the n_{app} and Q_{app} analysis above, we can infer a significant contribution from Coble creep. However, since a pure Coble creep mechanism would yield an n_{app}

of exactly 1, the observed $n_{app} \approx 1.5$ suggests the presence of other mechanisms, potentially dislocation slip or climb, which the method alone can neither definitively identify nor quantify. Similarly, at 1500 °C and 60 MPa, an n_{app} value of 7 and Q_{app} close to that of bulk diffusion (Q_l) might suggest dislocation climb as the predominant mechanism, yet the possibility of a combination with diffusional creep and dislocation slip cannot be dismissed.

Furthermore, several unanswered questions persist regarding the dependencies of the n_{app} and Q_{app} on temperature and stress. Firstly, what is the underlying reason responsible for the temperature dependence of the stress exponent? Specifically, why does n_{app} exhibit a non-monotonic trend with increasing temperature at stresses below 20 MPa? Moreover, why does Q_{app} exhibit a temperature dependence when the stress is lower than 10 MPa, but show constant values throughout the temperature range investigated at stress levels higher than 20 MPa? Secondly, what is the underlying reason for the stress dependence of Q_{app}? In particular, why Q_{app} shows a decreasing trend with increasing stress at temperature above 1100 °C? These intriguing and significant questions require further investigation.

The present physics-based model offers a robust complement to the conventional n_{app} and Q_{app} approach. It provides a clear picture of the relative activities of different creep mechanisms, as illustrated in the activity bar chart of Fig. 5. For the 1000 °C and 5 MPa scenario, the chart clarifies that the deviation of n_{app} from unity is primarily due to dislocation slip, with a smaller contribution from dislocation climb. Regarding another

case mentioned above, the 1500 °C and 60 MPa case, the relative activity bar chart provided in Fig. 5 shows unambiguously that dislocation climb contributes very little to the total creep strain. Instead, the total creep strain primarily arises from the dislocation slip. Thus, n_{app} ~7 together with Q_{app} close to the bulk diffusion, which once made us believe that the creep process was dominated by dislocation climb, actually result from the process of dislocations overcoming nanoparticles via thermally activated slip.

Regarding the first question about the temperature dependence of n_{app}, the relative activity data indicates that the underlying mechanism is the competition between the temperature effect on the relative activity of climb and that on intensity of dislocation-nanoparticles interaction. At stress levels below 20 MPa, the relative activity of dislocation climb increases with increasing temperature, at the expense of Coble creep. Since Coble creep has a theoretical stress exponent of unity and climb has a higher n value ranging from 5~7, when the relative activity of the former decreases whereas the latter increases, it is natural to see an increasing n_{app} with temperature. However, note that increasing the temperature also results in less intense interaction between the dislocations and nanoparticles, so the competition between these two effects leads to a non-monotonic behavior of n_{app} with temperature at stresses below 20 MPa. At high stress levels, as dislocation slip dominates the creep process with Coble and climb making very little contribution, the thermal energy barrier reduction owing to the rising temperature becomes the major factor, causing n_{app} to decrease monotonically with temperature, rather than showing a turning point as in cases where the stress is below 20 MPa.

This above-mentioned dislocation-particle interaction is also believed to be the reason for the decreasing trend of Q_{app} with increasing stress. More specifically, the dislocations overcome barriers via thermal activation, and the height of the barrier decreases with increasing stress [30]. Thus, when the stress increases, the energy barriers that the dislocations need to overcome become smaller, leading to the phenomenon of decreasing Q_{app} with increasing stress. Moreover, with increasing dislocation slip activity caused by increasing stress, the nanoparticles play more important roles during creep. An increasing frequency of dislocation-particle interaction leads to high values of n_{app}. This also explains the positive correlation between n_{app} and applied stress.

It's worth mentioning that the dislocation-nanoparticle interaction is usually characterized experimentally in a macroscopic sense as the threshold stress through fitting experimental data and extrapolating them to conditions where the creep rate is zero [66-68]. Many scholars have also proposed various mathematic expressions of the threshold stress in their research to rationalize the abnormally high creep stress exponent in alloys with high particle volume fractions [69-71]. Although some of them geniusly include the particle geometry descriptor into their formula [71], to date, the values of threshold stress still lack reliable and consistent expressions in a predictive sense [72]. In this study, however, instead of explicitly including the expression of threshold stress in our model, the dislocation-nanoparticle interaction is accounted for naturally via the thermal activation process of dislocations bypassing obstacles. This approach frees us from optimizing empirical parameters for the threshold stress evolution.

5.2 Parametric study: minimum acceptable grain size

The creep activities illustrated in Fig. 5 provide valuable guidance for modifying the Mo-La_2O_3 microstructures to serve under specific creep conditions. For instance, to enhance the creep properties of Mo-0.6wt%La_2O_3 at 10 MPa and 1000 °C, where Coble creep is the shortest board, it would be beneficial to add alloy elements that increase the grain boundary diffusion activation energy or simply adopt a coarser grain structure. For higher temperature conditions, such as 1500 °C, where dislocation slip and climb dominate the creep process, the strategy should shift to increasing the difficulty of dislocation motion. This can be achieved by adding elements that provide strong solution strengthening and precipitation hardening effects, along with increasing the formation and migration energy of vacancies within the Mo matrix. In scenarios involving extremely high stresses, like 120 MPa, simply slowing down diffusion processes might not yield significant benefits. Under these conditions, emphasis should be placed on strengthening the material by solute atoms or second phase particles.

While recommendations outlined provide a roadmap for microstructure design, they lack specifics on the degree to which these modifications should be implemented. Addressing this deficiency requires a detailed parametric study of microstructure descriptors to define the precise adjustments necessary for specific creep conditions. In the current study of the Mo-La_2O_3 alloy, this involves variations in grain size, particle size, particle number density, and dislocation density. To simplify, the size and number density of large particles are fixed at the values measured in Mo-0.6wt%La_2O_3, due to

their relatively smaller contribution compared to nanoparticles. The nanoparticle size is set at 100 nm to match typical values observed in Mo-0.6wt%La2O3 alloys. Detailed ranges for other microstructural features are specified in Table 6: grain sizes range from 5 to 100 μm, particle number densities from 10^{20} to 10^{21} m^{-3}, and dislocation densities in the cell interior from 10^{11} to 10^{12} m^{-2} per slip system (corresponding to a total dislocation density ranging from 2.64×10^{13} to 2.64×10^{14} m^{-2}, if assuming dislocation densities at subgrain boundaries are tenfold those within subgrains). The combination of these microstructure descriptors results in 252 (6×6×7) distinct virtual initial microstructures, each representative of achievable outcomes through typical large-scale industrial processes.

The predicted steady-state creep rates for the 252 virtual microstructures under various conditions are displayed in Fig. 6. Each grain size shows an upper and lower limit for the steady-state creep rates achievable through varying particle number density and dislocation density within reasonable ranges. Intriguingly, the upper limit for steady-state creep rates remains largely independent of grain size, while the lower limit escalates as grain size decreases. Fig. 6 also quantitatively reveal that the impact of grain size varies with the creep conditions: grain size effect becomes notably more pronounced at lower stress and temperature levels. For example, at 1200 °C and 90 MPa, increasing the average grain size from 20 μm to 100 μm reduces the lower limit of the steady-state creep rate by approximately 40%. However, at the same temperature with a reduced stress of 5 MPa, or at the same stress but at a lower temperature of 600 °C, the same increase in grain size results in a dramatic reduction of more than 95% in the lower limit. This creep-

condition-dependent grain size effect aligns with the effect of creep conditions on the relative activities of different creep mechanisms discussed in the previous subsection. Basically, creep conditions with lower stress and temperature are favorable for the activation of Coble creep whose strain rate is highly sensitive to the grain size, which therefore exacerbate the observed grain size effect.

One of the key insights from this parametric study is the introduction of the concept of "minimum acceptable grain size." While refining the grain structure is commonly recognized as beneficial for enhancing mechanical properties at room temperature, in high-temperature applications where creep resistance is paramount, too fine a grain structure can be detrimental. Therefore, when designing materials that must perform well under both high-temperature creep conditions and maintain good mechanical properties at room temperature, it is essential to find a grain size that balances these often conflicting requirements. The essence of this balance is to know how coarse the grain is coarse enough for creep to occur at a rate that is sufficiently low, or in other words, to determine a grain size that is coarse enough to optimize creep resistance without sacrificing too much the material's strength and ductility at ambient temperatures.

Fig. 6 illustrates that to achieve a specified steady-state creep rate, the grain size must surpass certain thresholds; otherwise, the desired performance is unattainable, regardless of adjustments to other microstructural descriptors such as particle number density and dislocation density. For instance, a steady-state creep rate lower than 10^{-11} s^{-1} at 1200 °C and 20 MPa cannot be achieved if the grain size is under 20 μm. Therefore, in such

scenarios, securing a grain size above this critical threshold should be a prerequisite before any other microstructural modifications are considered.

It's important to recognize that the minimum acceptable grain size is not a constant but varies with specific creep conditions. For example, a grain size of 20 μm, while inadequate for achieving the desired creep rate (10^{-11} s^{-1}) at 1200 °C and 20 MPa, is sufficiently coarse for less demanding conditions, such as lower stresses or temperatures. Notably, at temperatures below 800 °C, even a grain size as small as 5 μm is adequate across all stress levels studied, from 5 MPa to 120 MPa. This variability underscores that the minimum acceptable grain size depends critically on the specific operating conditions and targeted steady-state creep rate. This insight allows for the tailoring of grain size to meet specific service requirements, balancing high-temperature creep resistance with mechanical properties at ambient temperatures. Consequently, this forms a foundational element of sophisticated microstructural design strategies, accommodating a wide spectrum of operational conditions

5.3 Particle number density: more is better?

In addition to the grain size, another microstructure descriptor that plays an important role in the microstructure design is the geometry and number density of the second phase particles. While a higher number density of second phase particles generally boosts creep resistance, it often reduces ductility—a property crucial for formability and cost-effectiveness in manufacturing. This creates a trade-off akin to the grain size considerations discussed in subsection 5.2. Balancing these properties requires

identifying a particle number density that optimizes creep performance without excessively compromising ductility. To navigate this balance, a quantitative understanding on how particle density affects both room temperature ductility and steady-state creep rate under service conditions is crucial. Previous research, including multiscale strengthening and fracture models developed by our team, has detailed the impact of particle size and density on ductility in various alloys, such as aluminum [73-76], magnesium [77-79], and molybdenum [36, 37]. However, the quantitative effect on steady-state creep rate, especially under service conditions, remains under-explored, despite numerous experimental studies promoting the oversimplified belief that "more is better".

Insights into this issue can be gleaned from comparing the steady-state creep rates of Mo-La_2O_3 alloys with different nanoparticle densities under various conditions. As illustrated in Fig. 7(a), increasing nanoparticle density from ~1.0×10^{20} m^{-2} (Mo-0.6wt%La_2O_3) to 1.2×10^{20} m^{-2} (Mo-1.5wt%La_2O_3) does reduce the steady-state creep rate, but this effect is pronounced only at high temperature and stress conditions. At lower temperatures and stresses, the differences in creep rates between the two alloys are minimal. This suggests that the benefits of nanoparticle reinforcement in reducing creep rates are contingent upon the specific operational conditions of the alloy. Due to this reason, understanding the quantitative relationship between steady-state creep rate and particle number density should be a case-by-case analysis, tailored to specific creep conditions.

Fig. 7(b) illustrates under several distinct creep conditions how the steady-state creep rate of Mo-La_2O_3 alloys varies with the nanoparticle number density (assuming other microstructure descriptors being identical to those of Mo-0.6wt%La2O3). In each scenario, despite differences in stress and temperature, the steady-state creep rate is found to follow a common pattern: it decreases with increasing nanoparticle number density and then levels off once the density surpasses certain threshold values. These thresholds, however, are influenced by the specific creep conditions: both higher temperatures and stresses require higher nanoparticle number densities to achieve a leveling effect. Consequently, an increase in nanoparticle number density that might surpass the threshold under low stress and temperature conditions could still fall short of the threshold under more demanding conditions. This accounts for the observations in Figs. 7(a), where the steady-state creep rates in Mo-0.6wt%La_2O_3 and Mo-1.5wt%La_2O_3 alloys are similar under less demanding conditions but show significant discrepancies under tougher conditions, emphasizing the condition-dependent effectiveness of the nanoparticle reinforcement in the creep properties of Mo-La_2O_3 alloys.

This condition-dependent effectiveness challenges the common belief that "more is better." However, if more is not always better, the question then arises: what is the optimum particle number density? By plotting a horizontal line at a desired steady-state creep rate in Fig. 7(b) and finding where this line intersects the curve of steady-state creep rate versus particle number density, this value can be determined for each different creep condition of interest. For instance, to achieve a steady-state creep rate below 2×10^{-8} s^{-1} in a Mo-La_2O_3 alloy, the optimum number density for 100 nm La_2O_3 particles might be

3.6×10^{19} m^{-3} for 1200 °C and 50 MPa. This value increases to 3.2×10^{20} m^{-3} if the temperature is raised to 1300 °C while maintaining the same stress.

Applying this method across a wide range of creep conditions produces Fig. 7(c), which maps the necessary nanoparticle number density required under various conditions to keep a creep rate below 1×10^{-3} %/h. This figure illustrates that the required number density initially increases gradually with temperature and stress, then surges when the conditions become extreme. This indicates diminishing returns from further nanoparticle addition beyond a certain threshold, where their density becomes excessively high. In fact, simple math tells that for nanoparticles with a diameter of 100 nm, the number density of 0.95×10^{21} m^{-3} correspond to a volume fraction of ~50%, beyond which the alloy might no longer be considered a Mo-La_2O_3 alloy. In other words, any creep conditions requiring a nanoparticle number density exceeding this value are theoretically unattainable with La_2O_3 nanoparticles of 100 nm in diameter. For this reason, Fig. 7(d) reorganizes the data from Fig. 7(c) into three distinct zones. Zone 1 locates at places where both temperature and stress are low, denoted as unnecessary. In this zone, the material exhibits a steady-state creep rate below the desired steady state creep rate even without the addition of La_2O_3, indicating that no additional particles are needed. Zone 3 corresponds to creep conditions where both temperature and stress are high. This zone is denoted as impractical, as in this zone the calculated optimum particle number density exceeds practical limits, suggesting it is impossible to achieve the desired creep rate with a viable La_2O_3 content. Zone 2, denoted as achievable, covers the creep conditions between Zone 1 and Zone 3. In this intermediate zone, the optimal particle number density increases with rising

temperature and stress, showing a clear need for careful adjustment of particle number density to meet performance targets. This type of figure is useful in designing Mo-La_2O_3 alloys for specific service conditions, offering clear guidance on whether and how adjusting the number density of La_2O_3 nanoparticle might help achieve targeted steady-state creep rates.

Before wrapping up this subsection, it is important to emphasize that the particle densities depicted in Fig. 7(c) and (d) refer solely to nanoparticles and do not include larger particles that reside on grain boundaries. Therefore, these so called necessary nanoparticle number density should be regarded as a lower bound of the total particle number density present in the alloys. Actually, while the current model accounts for dislocation accumulation and annihilation, it does not incorporate the dynamics of recrystallization and grain growth. Consequently, the model is tailored to scenarios where the microstructure remains stable, typically ensured by the presence of micron-scale and submicron-scale particles. This limitation explains why the model fails to capture the high-temperature creep behavior of pure Mo accurately, as pure Mo lacks these stabilizing larger particles. This is also the reason why during parameter validation phase, we utilized only the initial creep rate of pure Mo instead of the whole creep curve to sidestep the complexities introduced by recrystallization and grain growth (Fig. 2). Looking forward, future works should focus on establishing physics models to consider the roles played by dislocation density and the geometry of large particles on recrystallization and grain growth, which affect the creep response of Mo alloys whose grain structure evolves during the creep processes.

6 Summary and conclusions

1) A physics-based creep model tailored to the unique hierarchical microstructure of Mo-La_2O_3 alloys has been developed. Through careful calibration—employing parameters sourced from the literature or adjusted within suggested limits—this model has proven capable of predicting the creep behavior of Mo-La_2O_3 alloys featuring varied microstructures, even under creep conditions that extend beyond those used for calibration.

2) The model effectively quantifies the relative activity of various creep mechanisms—such as dislocation slip, climb, Coble creep, and Nabarro-Herring creep—across different conditions. The predicted creep activities align with the results from the conventional analyses based on the value of apparent activation energy and stress exponent in scenarios dominated by a single creep mechanism. Crucially, the model clarifies the ambiguities associated with traditional approach in situations where multiple creep mechanisms contribute similarly. It also elucidates the intricate dependencies of apparent activation energy and stress exponent on varying creep conditions across a wide range.

3) For any given grain size, variations in other microstructural features result in a range of steady-state creep rates. The upper bound of this range is influenced by dislocation density and nanoparticle number density, while the lower bound is primarily determined by the grain size and decreases as the grain size increases. Thus, when designing Mo-La_2O_3 alloys to meet specific creep conditions where

the steady-state creep rate must remain below a certain threshold, it is crucial to first ensure that the grain size is sufficiently large such that the lower bound falls below this target rate. This establishes a minimum acceptable grain size, which can be derived from the model, and should be the initial consideration in microstructure design before considering adjustments to other microstructural features.

4) The enhancement of creep resistance through the addition of nanoparticles varies significantly with creep temperature and stress. Each creep condition is associated with a specific threshold nanoparticle number density, beyond which additional increases yield negligible benefits, suggesting more is not always better. The threshold value also varies depending on the creep condition, with harsher conditions requiring higher number densities. This is the reason why Mo alloys with varying La_2O_3 additions may perform similarly under mild conditions but exhibit divergent behaviors under more extreme conditions.

5) The model is capable of identifying the minimum nanoparticle number density required to maintain specific steady-state creep rates under various conditions. As the severity of the creep conditions increases, the minimum number density of nanoparticles may reach unrealistically high levels, suggesting that the desired performance levels might not be attainable with reasonable La_2O_3 additions. Conversely, under less demanding conditions of low stress and temperature, the model shows that Mo alloys can meet the creep performance criteria without

nanoparticle enhancement, thus negating the need for additional particles. This functionality of the model offers a valuable tool for assessing the practicality and necessity of nanoparticle additions to meet specific creep properties under conditions of interest.

Acknowledgments:

This work was supported by the National Natural Science Foundation of China (grant numbers 52371119, 51901173, U23A6013, 92360301, U2330203, 51801147, 51790482), the National Key Research and Development Program of China (No. 2017YFB0702301), and Shaanxi Province Innovation Team Project (No. 2024RS-CXTD-58).

Reference

[1] J.H. Perepezko, Materials science. The hotter the engine, the better, Science 326(5956) (2009) 1068-9.

[2] D.M. Dimiduk, J.H. Perepezko, Mo-Si-B alloys: Developing a revolutionary turbine-engine material, Mrs Bulletin 28(9) (2003) 639-645.

[3] J. Wadsworth, J. Wittenauer, The history of development of molybdenum alloys for structural applications, Lawrence Livermore National Lab., CA (United States), 1993.

[4] H. Walser, J.A. Shields, Traditional and emerging applications of molybdenum metal and its alloys, International Molybdenum Association, IMOA Newsletter 1 (2007) 16.

[5] M.S. El-Genk, J.-M. Tournier, A review of refractory metal alloys and mechanically alloyed-oxide dispersion strengthened steels for space nuclear power systems, Journal of Nuclear Materials 340(1) (2005) 93-112.

[6] H. Xing, P. Hu, C. He, X. Zhang, J. Han, F. Yang, R. Bai, W. Zhang, K. Wang, A.A. Volinsky, Design of high-performance molybdenum alloys via doping metal oxide and carbide strengthening: A review, Journal of Materials Science & Technology 160 (2023) 161-180.

[7] L. Xu, N. Li, W. Song, T. Sun, Y. Zhou, S. Wei, H. Shen, Achieving an unprecedented strength-ductility balance of molybdenum alloy by homogeneously distributing yttrium-cerium oxide, Journal of Alloys and Compounds 897 (2022) 163110.

[8] W. Hu, T. Sun, C. Liu, L. Yu, T. Ahamad, Z. Ma, Refined microstructure and enhanced mechanical properties in Mo-Y2O3 alloys prepared by freeze-drying method and subsequent low temperature sintering, Journal of Materials Science & Technology 88 (2021) 36-44.

[9] W. Hu, Z. Du, Z. Dong, L. Yu, T. Ahamad, Z. Ma, The synthesis of TiC dispersed strengthened Mo alloy by freeze-drying technology and subsequent low temperature sintering, Scripta Materialia 198 (2021) 113831.

[10] Z. Jiuxing, L. Lu, Z. Meiling, H. Yancao, Z. Tieyong, Fracture toughness of sintered Mo–La2O3 alloy and the toughening mechanism, International Journal of Refractory Metals and Hard Materials 17(6) (1999) 405-409.

[11] G.-j. Zhang, Y.-j. Sun, C. Zuo, J.-f. Wei, J. Sun, Microstructure and mechanical properties of multi-components rare earth oxide-doped molybdenum alloys, Materials Science and Engineering: A 483-484 (2008) 350-352.

[12] B.V. Cockeram, The Fracture Toughness and Toughening Mechanism of Commercially Available Unalloyed Molybdenum and Oxide Dispersion Strengthened Molybdenum with an Equiaxed, Large Grain Structure, Metallurgical and Materials Transactions A 40(12) (2009) 2843-2860.

[13] R. Bianco, R.W. Buckman Jr, C.B. Geller, High-strength, creep-resistant molybdenum alloy and process for producing the same, Google Patents, 1999.

[14] P.M. Cheng, C. Yang, P. Zhang, J.Y. Zhang, H. Wang, J. Kuang, G. Liu, J. Sun, Enhancing the high-temperature creep properties of Mo alloys via nanosized La2O3 particle addition, Journal of Materials Science & Technology 130 (2022) 53-63.

[15] B. Fischer, S. Vorberg, R. Völkl, M. Beschliesser, A. Hoffmann, Creep and tensile tests on refractory metals at extremely high temperatures, International Journal of Refractory Metals and Hard Materials 24(4) (2006) 292-297.

[16] R. Bianco, R. Buckman, Mechanical properties of oxide dispersion strengthened(ODS) molybdenum, Molybdenum and molybdenum alloys (1998) 125-142.

[17] J.-F. Wen, S.-T. Tu, F.-Z. Xuan, X.-W. Zhang, X.-L. Gao, Effects of Stress Level and Stress State on Creep Ductility: Evaluation of Different Models, Journal of Materials Science & Technology 32(8) (2016) 695-704.

[18] R. Browne, D. Lonsdale, P. Flewitt, Multiaxial stress rupture testing and compendium of data for creep resisting steels, (1982).
[19] Y.-K. Kim, D. Kim, H.-K. Kim, C.-S. Oh, B.-J. Lee, An intermediate temperature creep model for Ni-based superalloys, International Journal of Plasticity 79 (2016) 153-175.
[20] A. Narayanan, K. Dubey, C.M. Davies, J.P. Dear, The creep of alloy 617 at 700 °C: Material properties, measurement of strain and comparison between finite element analysis and digital image correlation, International Journal of Solids and Structures 129 (2017) 195-203.
[21] R. Evans, B. Wilshire, Creep behaviour of superalloy blade materials, Materials science and technology 3(9) (1987) 701-705.
[22] M.A. Kumar, L. Capolungo, Microstructure-sensitive modeling of high temperature creep in grade-91 alloy, International Journal of Plasticity 158 (2022) 103411.
[23] N. Bieberdorf, A. Tallman, M.A. Kumar, V. Taupin, R.A. Lebensohn, L. Capolungo, A mechanistic model for creep lifetime of ferritic steels: Application to Grade 91, International Journal of Plasticity 147 (2021) 103086.
[24] J. Coakley, D. Dye, H. Basoalto, Creep and creep modelling of a multimodal nickel-base superalloy, Acta Materialia 59(3) (2011) 854-863.
[25] B.F. Dyson, Microstructure based creep constitutive model for precipitation strengthened alloys: Theory and application, Materials Science and Technology 25(2) (2009) 213-220.
[26] D. Smirnova, S. Starikov, G.D. Leines, Y. Liang, N. Wang, M.N. Popov, I.A. Abrikosov, D.G. Sangiovanni, R. Drautz, M. Mrovec, Atomistic description of self-diffusion in molybdenum: A comparative theoretical study of non-Arrhenius behavior, Physical Review Materials 4(1) (2020).
[27] B. Bakó, E. Clouet, L.M. Dupuy, M. Blétry, Dislocation dynamics simulations with climb: kinetics of dislocation loop coarsening controlled by bulk diffusion, Philosophical Magazine 91(23) (2011) 3173-3191.
[28] Y. Gu, Y. Xiang, S.S. Quek, D.J. Srolovitz, Three-dimensional formulation of dislocation climb, Journal of the Mechanics and Physics of Solids 83 (2015) 319-337.
[29] J.P. Hirth, J. Lothe, T. Mura, Theory of dislocations, Journal of Applied Mechanics 50(2) (1983) 476-477.
[30] U.F. Kocks, A. As, A. Mf, Thermodynamics and kinetics of slip, (1975).
[31] S. Mukherjee, B. Zhou, A. Dasgupta, T.R. Bieler, Multiscale modeling of the anisotropic transient creep response of heterogeneous single crystal SnAgCu solder, International Journal of Plasticity 78 (2016) 1-25.
[32] S. Wu, H.Y. Song, H.Z. Peng, P.D. Hodgson, H. Wang, X.H. Wu, Y.M. Zhu, M.C. Lam, A.J. Huang, A microstructure-based creep model for additively manufactured nickel-based superalloys, Acta Materialia 224 (2022) 117528.
[33] W. Wen, L. Capolungo, C.N. Tomé, Mechanism-based modeling of solute strengthening: Application to thermal creep in Zr alloy, International Journal of Plasticity 106 (2018) 88-106.
[34] G. Liu, G.J. Zhang, F. Jiang, X.D. Ding, Y.J. Sun, J. Sun, E. Ma, Nanostructured high-strength molybdenum alloys with unprecedented tensile ductility, Nat Mater 12(4) (2013) 344-50.
[35] Y. Chen, Y. Fang, P. Cheng, X. Ke, M. Zhang, J. Zou, J. Ding, B. Zhang, L. Gu, Q. Zhang, G. Liu, Q. Yu, The origin of exceptionally large ductility in molybdenum alloys dispersed with irregular-shaped La(2)O(3) nano-particles, Nat Commun 15(1) (2024) 4105.
[36] P. Cheng, S. Wu, P. Zhang, J. Kuang, H. Wang, G. Liu, J. Sun, Ductilizing Mo alloys via nanoparticle-stabilized microstructural hierarchy, Materials Research Letters 11(1) (2022) 90-98.
[37] P.M. Cheng, S.L. Li, G.J. Zhang, J.Y. Zhang, G. Liu, J. Sun, Ductilizing Mo–La 2 O 3 alloys with ZrB 2 addition, Materials Science and Engineering: A 619 (2014) 345-353.

[38] P.M. Cheng, Z.J. Zhang, G.J. Zhang, J.Y. Zhang, K. Wu, G. Liu, W. Fu, J. Sun, Low cycle fatigue behaviors of pure Mo and Mo-La2O3 alloys, Materials Science and Engineering: A 707 (2017) 295-305.
[39] G.J. Zhang, Y.J. Sun, R.M. Niu, J. Sun, J.F. Wei, B.H. Zhao, L.X. Yang, Microstructure and strengthening mechanism of oxide lanthanum dispersion strengthened molybdenum alloy, Advanced Engineering Materials 6(12) (2004) 943-948.
[40] G.-j. Zhang, G. Liu, Y.-j. Sun, F. Jiang, L. Wang, R. Wang, J. Sun, Microstructure and strengthening mechanisms of molybdenum alloy wires doped with lanthanum oxide particles, International Journal of Refractory Metals and Hard Materials 27(1) (2009) 173-176.
[41] P.M. Cheng, G.J. Zhang, J.Y. Zhang, G. Liu, J. Sun, Coupling effect of intergranular and intragranular particles on ductile fracture of Mo–La2O3 alloys, Materials Science and Engineering: A 640 (2015) 320-329.
[42] R. Lebensohn, C. Tomé, A self-consistent anisotropic approach for the simulation of plastic deformation and texture development of polycrystals: application to zirconium alloys, Acta metallurgica et materialia 41(9) (1993) 2611-2624.
[43] H. Wang, L. Capolungo, B. Clausen, C.N. Tomé, A crystal plasticity model based on transition state theory, International Journal of Plasticity 93 (2017) 251-268.
[44] H. Wang, B. Clausen, L. Capolungo, I.J. Beyerlein, J. Wang, C.N. Tomé, Stress and strain relaxation in magnesium AZ31 rolled plate: In-situ neutron measurement and elastic viscoplastic polycrystal modeling, International Journal of Plasticity 79 (2016) 275-292.
[45] A. Granato, K. Lücke, J. Schlipf, L. Teutonico, Entropy factors for thermally activated unpinning of dislocations, Journal of Applied Physics 35(9) (1964) 2732-2745.
[46] C. Sobie, N. Bertin, L. Capolungo, Analysis of obstacle hardening models using dislocation dynamics: application to irradiation-induced defects, Metallurgical and Materials Transactions A 46(8) (2015) 3761-3772.
[47] Y. Dong, T. Nogaret, W.A. Curtin, Scaling of Dislocation Strengthening by Multiple Obstacle Types, Metallurgical and Materials Transactions A 41(8) (2010) 1954-1960.
[48] K.-S. Wang, J.-F. Tan, P. Hu, Z.-T. Yu, F. Yang, B.-L. Hu, R. Song, H.-C. He, A.A. Volinsky, La2O3 effects on TZM alloy recovery, recrystallization and mechanical properties, Materials Science and Engineering: A 636 (2015) 415-420.
[49] U. Kocks, H. Mecking, Physics and phenomenology of strain hardening: the FCC case, Progress in materials science 48(3) (2003) 171-273.
[50] Y. Estrin, Dislocation theory based constitutive modelling: foundations and applications, Journal of Materials Processing Technology 80-81 (1998) 33-39.
[51] R.A. Lebensohn, C.S. Hartley, C.N. Tomé, O. Castelnau, Modeling the mechanical response of polycrystals deforming by climb and glide, Philosophical Magazine 90(5) (2010) 567-583.
[52] G.S. Was, Fundamentals of radiation materials science: metals and alloys, Springer2007.
[53] M.G.D. Geers, M. Cottura, B. Appolaire, E.P. Busso, S. Forest, A. Villani, Coupled glide-climb diffusion-enhanced crystal plasticity, Journal of the Mechanics and Physics of Solids 70 (2014) 136-153.
[54] R. Coble, A model for boundary diffusion controlled creep in polycrystalline materials, Journal of applied physics 34(6) (1963) 1679-1682.
[55] F. Nabarro, Report on strength of solids, Physical Society (1948) 38.
[56] C. Herring, Diffusional viscosity of a polycrystalline solid, Journal of applied physics 21(5) (1950) 437-445.
[57] H.J. Frost, M. Ashby, Deformation-mechanism maps: The plasticity and creep of metals and

ceramics(Book), Oxford, Pergamon Press, 1982, 175 p (1982).
[58] K. Jing, R. Liu, Z.M. Xie, J.G. Ke, X.P. Wang, Q.F. Fang, C.S. Liu, H. Wang, G. Li, X.B. Wu, Excellent high-temperature strength and ductility of the ZrC nanoparticles dispersed molybdenum, Acta Materialia 227 (2022) 117725.
[59] A. Patra, D.L. McDowell, Crystal plasticity-based constitutive modelling of irradiated bcc structures, Philosophical Magazine 92(7) (2012) 861-887.
[60] W. Li, H. Kou, X. Zhang, J. Ma, Y. Li, P. Geng, X. Wu, L. Chen, D. Fang, Temperature-dependent elastic modulus model for metallic bulk materials, Mechanics of Materials 139 (2019) 103194.
[61] L. Hollang, D. Brunner, A. Seeger, Work hardening and flow stress of ultrapure molybdenum single crystals, Materials Science and Engineering: A 319 (2001) 233-236.
[62] L. Hollang, M. Hommel, A. Seeger, The Flow Stress of Ultra‐High‐Purity Molybdenum Single Crystals, Physica status solidi (a) 160(2) (1997) 329-354.
[63] K. Maier, H. Mehrer, G. Rein, Self-diffusion in molybdenum, International Journal of Materials Research 70(4) (1979) 271-276.
[64] J. Cadek, Creep in metallic materials, Materials science monographs 48 (1988).
[65] W. Wen, L. Capolungo, A. Patra, C.N. Tomé, A Physics-Based Crystallographic Modeling Framework for Describing the Thermal Creep Behavior of Fe-Cr Alloys, Metallurgical and Materials Transactions A 48(5) (2017) 2603-2617.
[66] Y. Zhao, Q. Fang, Y. Liu, P. Wen, Y. Liu, Creep behavior as dislocation climb over NiAl nanoprecipitates in ferritic alloy: The effects of interface stresses and temperature, International Journal of Plasticity 69 (2015) 89-101.
[67] S. Zhu, S. Tjong, J. Lai, Creep behavior of a β′ (NiAl) precipitation strengthened ferritic Fe–Cr–Ni–Al alloy, Acta materialia 46(9) (1998) 2969-2976.
[68] C. Stallybrass, A. Schneider, G. Sauthoff, The strengthening effect of (Ni, Fe) Al precipitates on the mechanical properties at high temperatures of ferritic Fe–Al–Ni–Cr alloys, Intermetallics 13(12) (2005) 1263-1268.
[69] E. Arzt, M.F. Ashby, Threshold stresses in materials containing dispersed particles, (1982).
[70] B. Reppich, On the attractive particle–dislocation interaction in dispersion-strengthened material, Acta materialia 46(1) (1998) 61-67.
[71] J. Rösler, E. Arzt, The kinetics of dislocation climb over hard particles—I. Climb without attractive particle-dislocation interaction, Acta Metallurgica 36(4) (1988) 1043-1051.
[72] M.A. Muñoz-Morris, I. Gutierrez-Urrutia, D.G. Morris, Influence of nanoprecipitates on the creep strength and ductility of a Fe–Ni–Al alloy, International Journal of Plasticity 25(6) (2009) 1011-1023.
[73] G. Liu, J. Sun, C.-W. Nan, K.-H. Chen, Experiment and multiscale modeling of the coupled influence of constituents and precipitates on the ductile fracture of heat-treatable aluminum alloys, Acta Materialia 53(12) (2005) 3459-3468.
[74] G. Liu, G. Zhang, X. Ding, J. Sun, K. Chen, The influences of multiscale-sized second-phase particles on ductility of aged aluminum alloys, Metallurgical and Materials Transactions A 35(6) (2004) 1725-1734.
[75] G. Liu, G. Zhang, R. Wang, W. Hu, J. Sun, K. Chen, Heat treatment-modulated coupling effect of multi-scale second-phase particles on the ductile fracture of aged aluminum alloys, Acta Materialia 55(1) (2007) 273-284.
[76] J. Kuang, X. Zhao, Y. Zhang, J. Zhang, G. Liu, J. Sun, G. Xu, Z. Wang, Impact of thermal exposure on the microstructure and mechanical properties of a twin-roll cast Al-Mn-Fe-Si strip, Journal of Materials Science & Technology 107 (2022) 183-196.

[77] W. Fu, R. Wang, K. Wu, J. Kuang, J. Zhang, G. Liu, J. Sun, The influences of multiscale second-phase particles on strength and ductility of cast Mg alloys, Journal of Materials Science 54(3) (2018) 2628-2647.
[78] W. Fu, R. Wang, J. Zhang, K. Wu, G. Liu, J. Sun, The effect of precipitates on voiding, twinning, and fracture behaviors in Mg alloys, Materials Science and Engineering: A 720 (2018) 98-109.
[79] W. Fu, R.H. Wang, H. Xue, J. Kuang, J.Y. Zhang, G. Liu, J. Sun, Effects of Zr addition on the multi-scale second-phase particles and fracture behavior for Mg-3Gd-1Zn alloy, Journal of Alloys and Compounds 747 (2018) 197-210.

Table 1 Microstructure descriptors extracted from experiments

Material	Intragranular				Intergranular		grain
	Nanopaticles		Submicron-scale particles		Micron-scale particles		Average diameter
	N_p^{cell} (m^{-3})	D_p^{cell} (nm)	N_p^{cw}(nm)	D_p^{cw} (nm)	N_p^{gb}(m^{-3})	D_p^{gb} (μm)	D (μm)
Mo-0.6wt.%La_2O_3	1.0×10^{20}	65.5	1.3×10^{17}	382.5	1.1×10^{16}	0.82	41
Mo-0.9wt.%La_2O_3	1.1×10^{20}	71.8	1.5×10^{17}	415.3	1.9×10^{16}	0.87	54
Mo-1.5wt.%La_2O_3	1.2×10^{20}	73.5	3.4×10^{17}	395.3	1.6×10^{16}	1.02	51

Table 2 The calibrated parameter values used for the Mo-La_2O_3

Parameter	value	Suggested Range	Source
b(magnitude of Burgers vector)	2.73×10^{-10} m	-	[58]
V (Gaussien distribution variance)	100 MPa^2	10~1000 MPa^2	Fitted
h_p (Precipitation hardening coefficient)	0.64	0~1	Fitted
ρ_{cell}^s (initial mobile dislocation in each slip system)	3×10^{11} m^{-2}	10^{11}~10^{12} m^{-2}	Fitted
ρ_{cw}^s (initial cell wall dislocation density in each slip system)	3.5×10^{12} m^{-2}	3~20×ρ_{cell}^s	Fitted
$\alpha^{ss'}$ (latent hardening matrix)	0.7 (collinear); 0.3 (non-collinear)	0~1	[46, 59]*
m (hardening superposition parameter)	2	1~2	[47]
μ (shear modulus)	$131983 - 20.24 \times T$ MPa	-	[60]*
τ_0 (lattice friction at $T > 600$ ℃)	0 MPa	-	[61, 62]
$\Delta G_{0,\rho}$ (zero stress activation energy for dislocations)	7.2 eV	0~10 eV	Fitted
$\Delta G_{0,p}$ (zero stress activation energy for precipitates)	8.5 eV	1~2×$\Delta G_{0,\rho}$	Fitted
p (exponent parameter)	0.667	0~1	[30]*
q (exponent Parameter)	1.5	1~2	[30]*
υ_P (attempt frequency for precipitation obstacles)	1×10^{11} s^{-1}	10^{10}~10^{11} s^{-1}	[59]*
k_1 (material constant)	0.02	-	Fitted
k_2 (material constant)	80	-	Fitted
n_0 (annihilation strain rate sensitivity)	4.5	3~5	[50]*
Q_l (diffusion activation energy in the lattice)	4.78 eV	-	[63]
Q_{gb} (diffusion activation energy along grain boundaries)	3.3 eV	0~Q_l	[57]*
D_0 (diffusivity pre-factor)	10^{-4} m^2s^{-1}	-	[26]
α_{coble} (Coble creep constant)	148	-	[64]
α_{N-H} (N-H creep constant)	15	-	[64]
δ_{gb} (grain boundary thickness)	0.7 nm	-	[23]
r_d (inner radius of dislocation control volume)	4b	-	[53]
r_∞ (outer radius of dislocation control volume)	200b	-	[65]

*Parameter estimated or back-fitted using the data provided in the given references.

Table 3 creep stress exponent of Mo-0.6wt%La_2O_3 at various creep conditions

Temperature (℃)	n_{app}				
	5 MPa	10 MPa	20 MPa	60 MPa	120 MPa
1000 ℃	1.54	1.84	3.24	9.28	17.22
1100 ℃	1.78	2.10	3.38	8.89	16.25
1200 ℃	1.83	2.17	3.36	8.53	15.35
1300 ℃	1.80	2.14	3.28	8.14	14.51
1400 ℃	1.74	2.09	3.18	7.78	13.74
1500 ℃	1.69	2.03	3.07	7.42	13.02

Table 4 creep stress exponent of Mo-1.5wt%La_2O_3 at various creep conditions

Temperature (℃)	n_{app}				
	5 MPa	10 MPa	20 MPa	60 MPa	120 MPa
1000 ℃	1.35	1.42	2.33	9.55	17.35
1100 ℃	1.66	2.13	3.50	9.21	16.38
1200 ℃	1.88	2.00	2.98	8.82	15.48
1300 ℃	1.90	2.06	3.03	8.42	14.64
1400 ℃	1.83	2.04	2.99	8.03	13.86
1500 ℃	1.75	2.00	2.93	7.67	13.13

Table 5 Apparent creep activation energy for Mo-0.6wt% La_2O_3 and Mo-1.5wt% La_2O_3 at various stress levels

	Q_{app} (KJ/mol)	
	Mo-0.6wt% La2O3	Mo-1.5wt% La2O3
5 MPa	507.4	521.9 (1200~1500 ℃); 221.9 (1000~1100 ℃)
10 MPa	503.8	524.6 (1200~1500 ℃); 252.6 (1000~1100 ℃)
20 MPa	502.1	515.7
60 MPa	435.6	446.3
120 MPa	350.2	362.7

Table 6 Considered ranges of microstructure parameters used in the parametric study.

Microstructure descriptor	Values
ρ_{cell}^{s} (m^{-2})	[1, 2, 4, 6, 8, 10]×10^{11}
N_p^{cell} (m^{-3})	[1, 2, 4, 6, 8, 10]×10^{20}
D (μm)	[5, 10, 20, 40, 60, 80, 100]

Figures with captions

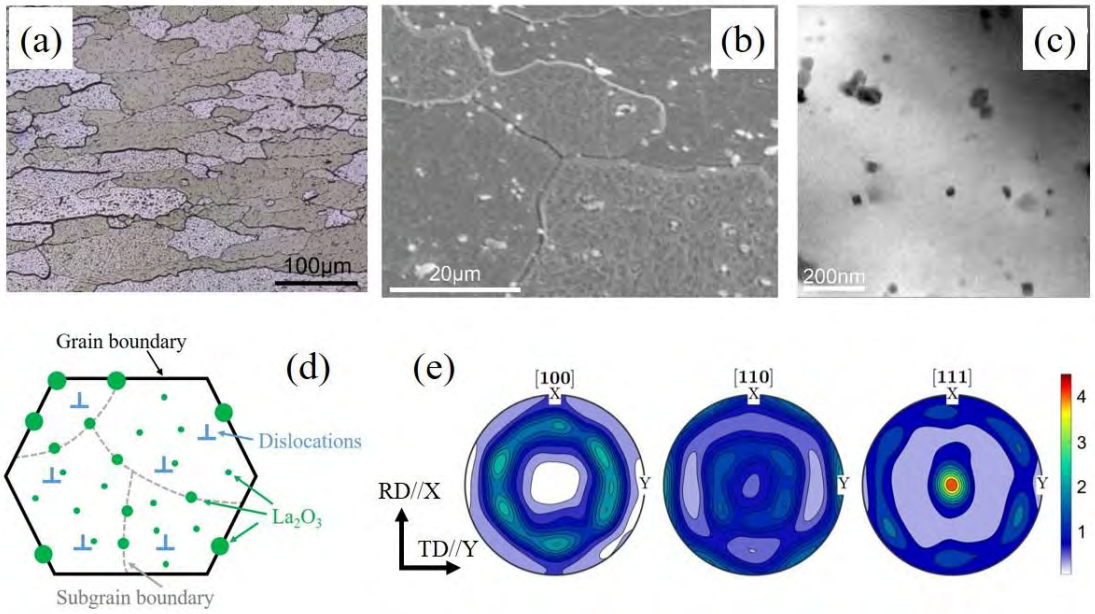

Fig. 1 Representative Microstructrue of Mo-La_2O_3 alloys: (a) optical microstructrue showing the grain morphology; (b) SEM secondary electron image highlighting the presence of micron-scale and submicron-scale La_2O_3 particles dispersed within the Mo matrix; (c) TEM bright-field image showing the La_2O_3 nanoparticles. (d) schemetics illustrating the characteristic hierarchical microstructure of Mo-La_2O_3 alloys; (e) {100}, {110} and {111} pole figures displaying the typical BCC rolling texture of the Mo matrix.

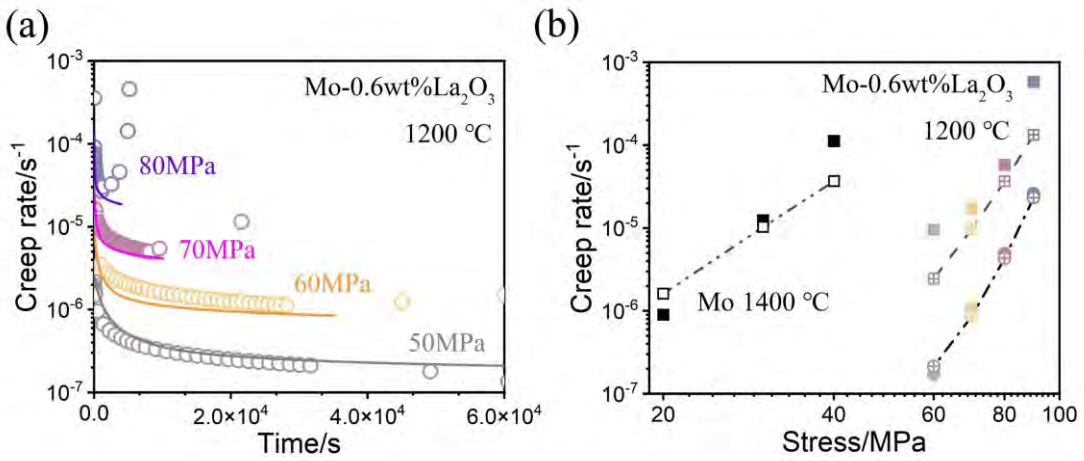

Fig. 2 Parameter calibration and validation: (a) fitted creep curves (solid lines) alongside the measured data (empty circles) for Mo-0.6wt%La2O3 at 1200 °C under different stress levels; (b) comparison of simulated and measured initial creep rates and steady-state creep rates. The fitting was performed using data from Mo-0.6wt%La_2O_3 at 1200 °C with stresses ranging from 50 MPa to 80 MPa. The black data point in (b) is used for validation only.

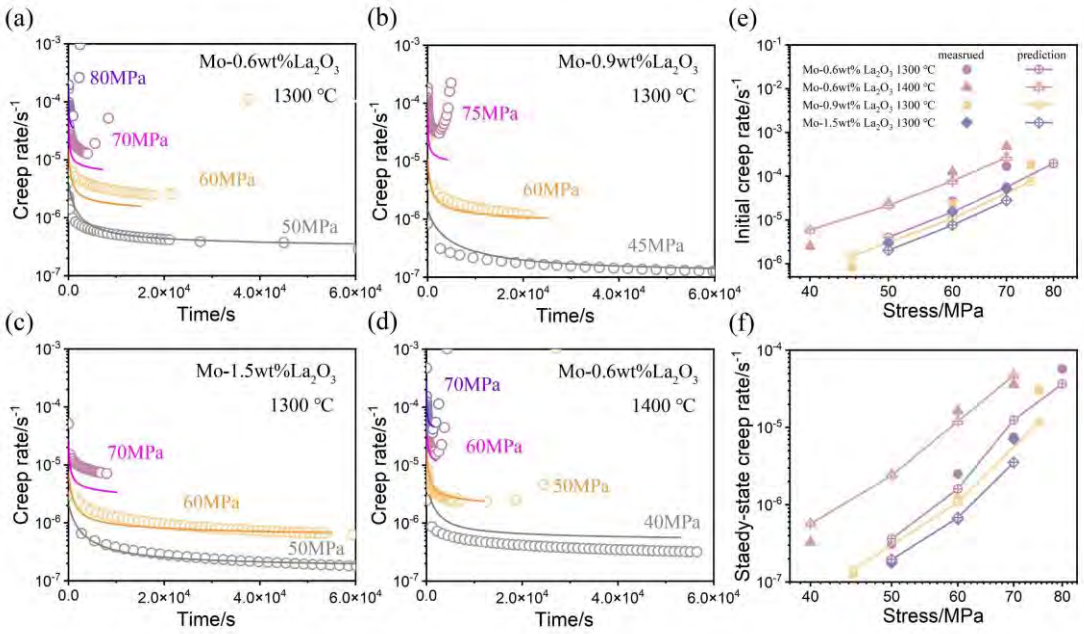

Fig. 3 Creep behavior predictions given by the present model: (a~d) simulated and measured creep curves: (a) Mo-0.6wt%La_2O_3 at 1300 °C; (b) Mo-0.9wt%La_2O_3 at 1300 °C; (c) Mo-1.5wt%La_2O_3 at 1300 °C; (d) Mo-0.6wt%La_2O_3 at 1400 °C. (e) comparison of simulated and measured initial creep rates; (f) Comparison of simulated and measured steady-state creep rates.

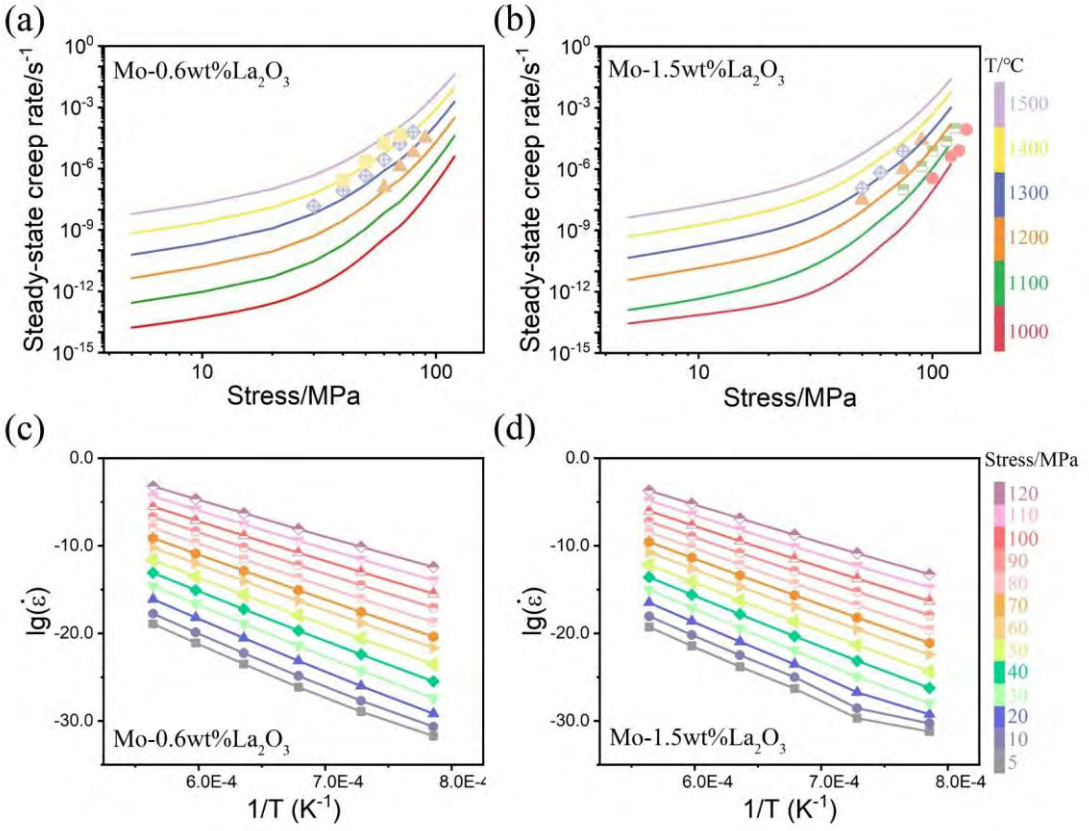

Fig. 4 Apparent creep stress exponent and activation energy: (a) and (b) steady-state creep rate versus stress in double logarithmic scale; (c) and (d) Logarithm of steady-state creep rate versus reciprocal temperature. (a) and (c) correspond to Mo-0.6wt%La_2O_3; (b) and (d) correspond to Mo-1.5wt%La_2O_3.

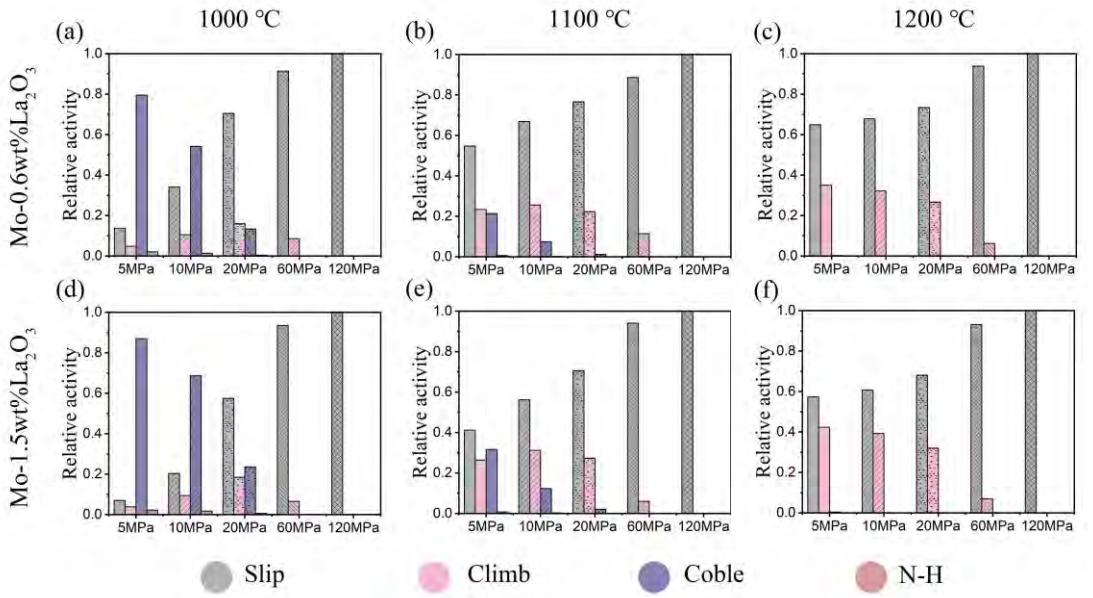

Fig. 5 Relative activities of different creep mechanisms under representative creep conditions: (a~c) Mo-0.6wt%La_2O_3, (d~e) Mo-1.5wt%La_2O_3; (a) and (d) correspond to creep at 1000 ℃, (b) and (e) 1100 ℃; (c) and (f) 1200 ℃.

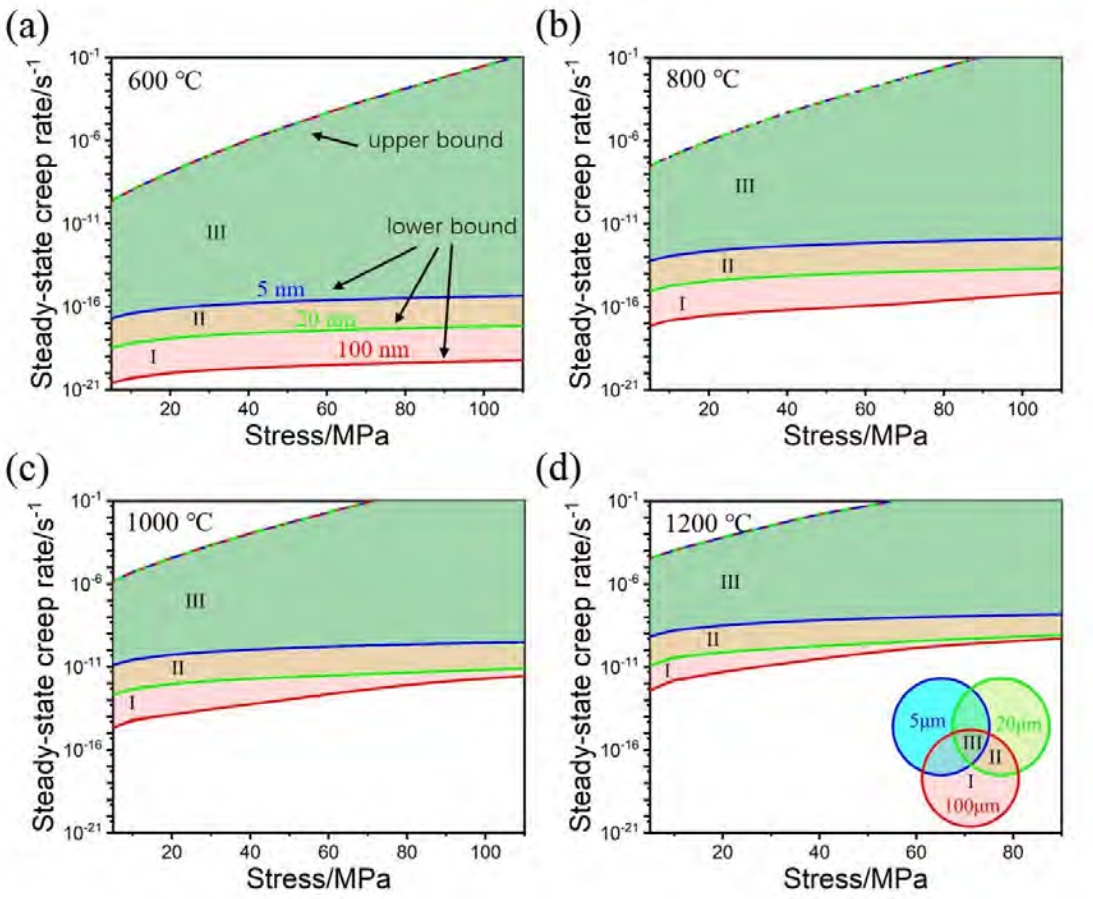

Fig. 6 Parametric studies on the microstructure descriptors: (a) 600 °C; (b) 800 °C; (c) 1000 °C; (d) 1200 °C. For each temperature, 252 virtual microstructures are considered. The shaded regions indicate the spread in the steady-state creep rate of the material with a given grain size, due to variations in other microstructure descriptors. The upper bounds of the shaded regions are represented by dashed lines, and the lower bounds by solid lines. Different colors correspond to different grain sizes.

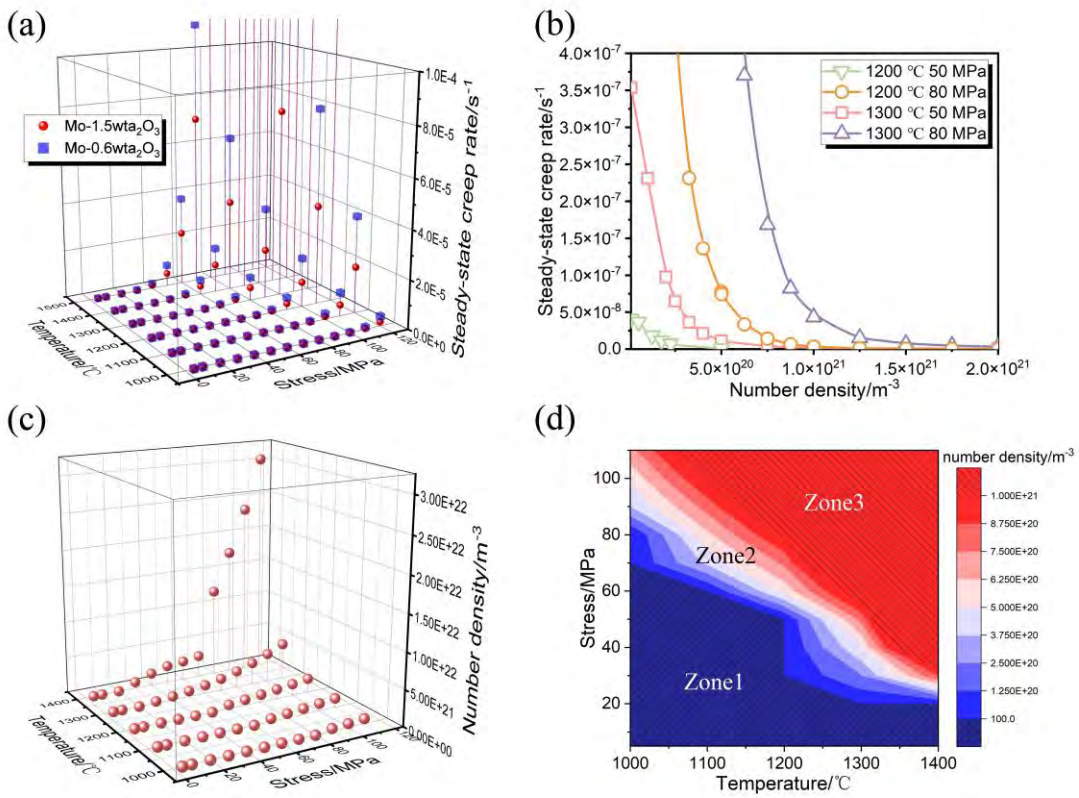

Fig. 7 Analysis of the effect of nanoparticle number density on the steady-state creep rate and its implications on material design: (a) Comparison of steady-state creep rates for Mo-0.6wt%La_2O_3 and Mo-1.5wt%La_2O_3 under various creep conditions; (b) Variation of steady-state creep rates with nanoparticle number density for different creep conditions; (c) necessary nanoparticle number density under various creep conditions to achieve a steady-state creep rate below 1×10^{-3} %/h; (d) Contour maps from (c) showing the creep parameter space (temperature and stress) divided into three zones: unnecessary (Zone 1), achievable (Zone 2), and impractical (Zone 3).